Spatial and Temporal Changes in Choroid Morphology Associated With Long-Duration Spaceflight

Charles Bélanger Nzakimuena,[1] Marissé Masís Solano,[1,2] Rémy Marcotte-Collard,[3] Mark Richard Lesk,[1,2] and Santiago Costantino[1,2]

[1]Centre de Recherche de l'Hôpital Maisonneuve-Rosemont, Montréal, Québec, Canada
[2]Département d'ophtalmologie, Faculté de Médecine, Université de Montréal, Montréal, Québec, Canada
[3]École d'optométrie, Université de Montréal, Montréal, Québec, Canada

Correspondence: Santiago Costantino, Centre de Recherche de l'Hôpital Maisonneuve-Rosemont, 5415 l'Assomption, Montréal, QB H1T 2M4, Canada; santiago.costantino@umontreal.ca.

Received: October 1, 2024
Accepted: April 14, 2025
Published: May 7, 2025

Citation: Bélanger Nzakimuena C, Masís Solano M, Marcotte-Collard R, Lesk MR, Costantino S. Spatial and temporal changes in choroid morphology associated with long-duration spaceflight. *Invest Ophthalmol Vis Sci.* 2025;66(5):17. https://doi.org/10.1167/iovs.66.5.17

Purpose. Amid efforts to understand spaceflight associated neuro-ocular syndrome (SANS), uncovering the role of the choroid in its etiology is challenged by the accuracy of image segmentation. The present study extended deep learning–based choroid quantification from optical coherence tomography (OCT) to the characterization of pulsatile and topological changes in the macular plane and investigated changes in response to prolonged microgravity exposure.

Methods. We analyzed OCT macular videos and volumes acquired from astronauts before, during, and after long-duration spaceflight. Deep learning models were fine-tuned for choroid segmentation and combined with further image processing toward vascularity quantification. Statistical analysis was performed to determine changes in time-dependent and spatially averaged variables from preflight baseline.

Results. For 12 astronauts with a mean age of 47 ± 9 years, there were significant increases in choroid thickness and luminal area (LA) averaged over OCT macular video segments. There was also a significant increase in pulsatile LA. For a subgroup of six astronauts for whom inflight imaging was available, choroid volume, luminal volume, and the choroidal vascularity index over the macular region all increased significantly during spaceflight.

Conclusions. The findings suggest that localized choroid pulsatile changes occur following prolonged microgravity exposure. They show that the choroid vessels expand in a manner similar to the choroid layer across the macular region during spaceflight, with a relative increase in the space they occupy. The methods developed provide new tools and avenues for studying and establishing effective countermeasures to risks associated with long-duration spaceflight.

Keywords: optical coherence tomography, choroid, deep learning, spaceflight-associated neuro-ocular syndrome, microgravity

Following prolonged exposure to microgravity, astronauts present with distinct neuro-ophthalmic findings collectively referred to as spaceflight associated neuro-ocular syndrome (SANS).[1,2] The signs defining SANS include unilateral and bilateral optic disc edema, posterior globe flattening, choroidal and retinal folds, hyperopic refractive error shifts, retinal nerve fiber layer infarcts, increased peripapillary total retinal thickness from the Bruch's membrane opening to 250 µm, and increased cerebrospinal fluid volume in optic nerve sheaths.[1–8] Although there have not been reports of permanent vision loss as a result of SANS, severe optic disc edema could damage visual pathways to the brain, and it has been identified as the chief risk associated with SANS.[7] Choroidal tissue undergoes acute variations in space over time,[9] and finite element modeling of the posterior segment of the eye suggests that increased pulsatile choroid volume fluctuation may elevate strains in prelaminar neural tissue. The increased strains could in turn lead to the development of edema.[2,10]

Pulsatile choroid volume fluctuation has been used to compute ocular rigidity and evaluate its response to long-duration spaceflight.[11] The effect of microgravity exposure on pulsatile choroid volume fluctuation itself has not yet been scrutinized. However, there is evidence that the choroid expands as soon as it is exposed to microgravity,[2,6,12] and the peripapillary choroid remains thicker than the pre-spaceflight baseline for at least 30 days and up to 90 days after landing.[2,6] The view that choroidal swelling may be in part responsible for the hyperopic shifts and choroidal folds observed in SANS[3–5,13] and the possible link between altered choroid pulsatility and edema warrant seeking a refined characterization of choroidal changes in response to microgravity.

The development of optical coherence tomography (OCT) with enhanced depth imaging has made possible the visualization of details of the choroid in most imaged subjects[9] and enabled the performance of reproducible biometric measurements.[9,14,15] Several means of quanti-

fying the morphology of the choroid from OCT representations have been devised.[16] Albeit routinely resorted to in clinical research contexts, manual segmentation of the choroid is labor intensive[17–19] and ill suited for the considerable volume of data produced by OCT devices, entailing a pace vastly exceeded by recent automated approaches.[18] The automated choroid semantic segmentation landscape has evolved from the use of various classical image processing methods[20,21] to the application of deep neural networks.[19] Under the supervised deep learning paradigm, the transformer architecture has demonstrated superior capabilities compared to convolutional neural networks when applied to computer vision tasks, including segmentation.[22,23]

Within the context of choroid segmentation, a few methods enable the differentiation of vasculature lumen and walls. It is now possible to identify, within a single OCT B-scan, the luminal area (LA) and to calculate choroidal vascularity index (CVI), defined as the fraction of LA over the total choroid area. However, the successful application of such parameters is highly dependent upon the accurate delineation of the choroid.[24]

There is a correlation between pulsatile choroid volume fluctuation and ocular rigidity,[25] and ocular rigidity has been reported to decrease in response to microgravity exposure.[11,12] We hypothesized that structural choroidal vascular changes in the macular region could be quantified, and we analyzed OCT-based spatial and temporal changes in the choroid morphology of astronauts during and following long-duration space missions.

For the present work, we trained deep learning models to reliably produce choroid semantic segmentations in macular images from OCT videos and OCT volumes acquired from astronauts. We complemented our segmentation techniques with vascularity quantification, enhancing the ability to characterize the state of the choroid and its variations. We extended the capability of our approaches to OCT image time series and OCT volume reconstructions. For video acquisitions, we compared pre- and post-spaceflight quantifications and revealed significant changes in time-dependent variables. For volumes, we captured substantial mapping changes over several time points in a cohort of astronauts exposed to microgravity.

Methods

Datasets

The study was approved by the institutional review boards of the Maisonneuve-Rosemont Hospital and National Aeronautics and Space Administration (NASA) and the clinical research ethics committee of Université de Montréal, and it was conducted according to the tenets of the Declaration of Helsinki. Two datasets were used (see Supplementary Table S1 for a summary). All acquisitions were performed using spectral-domain OCT (SPECTRALIS OCT2; Heidelberg Engineering, Heidelberg, Germany). Study participation required not having received any previous glaucoma-related surgeries, and none was reported. No ocular pathologies were identified prior to spaceflight in any of the subjects participating in the study based on OCT and fundus examination.

OCT macular videos were obtained through a specialized feature complementary to the acquisition software of the OCT device, which was provided to us by Heidelberg Engineering. The videos were acquired pre- and post-spaceflight from both eyes in the enhanced depth imaging mode, with up to five videos per eye at each time point. Each frame has dimensions 768 × 496 pixels, approximately corresponding to 8.4 × 1.9 mm, and each video was roughly 1 minute in length. Each OCT video was acquired along a macular plane segment centered at the fovea. The segment was rotated bidirectionally to within 15° to 45° from the horizontal (nasal to temporal direction) about the fovea, based on a trained operator's visual assessment of the quality of the displayed frame. The operator's quality optimization was performed at each acquisition independently. Video acquisitions had a specified automatic real time frame averaging of 5 or 10 frames. A resting heart rate measurement was also obtained concurrently with video acquisition.

For the analysis of changes in three-dimensional topology due to microgravity exposure, we used a set of OCT macular volumes composed of 97 or 193 B-scans. The macula block setting was used with placement over the fovea via the anatomic positioning system for each acquisition. For each time point, up to two volumes per eye were obtained in the enhanced depth imaging mode. All frames in the set of OCT macular volumes measured 512 × 496 pixels, which physically is approximately 5.6 × 1.9 mm.

Segmentation Training and Performance Evaluation

SegFormer models[26] pretrained on the ImageNet database were retrained directly on both datasets toward choroid segmentation. For OCT videos, training data were gathered by randomly selecting 10 B-scans per movie for a total training dataset of 1070 B-scans, where the choroid region was manually labeled by one trained grader and binarized. For OCT volumes, we devised a strategy to ensure adequate representation of the distribution of B-scans corresponding to each subject's eye in the training data. The image set was split into five groups along the slow acquisition direction, and four B-scans from each group were randomly selected for a total of 20 per volume. For each volume, four B-scans out of 20 were manually labeled by one trained grader and binarized. The locations of the labeled B-scans were subsequently shifted as shown in Supplementary Figure S9, resulting in a training dataset of 260 B-scans.

The training of the SegFormer models was achieved through the use of intersection over union (IoU) loss. For binary segmentation, which was used exclusively in the present study, the IoU equation is given by Equation 1:

$$\mathcal{L}_{IoU} = 1 - \frac{\sum_{i=1}^{N} g_i s_i}{\sum_{i=1}^{N} \left(g_i + s_i - g_i s_i\right)} \quad (1)$$

where $\mathcal{L}_{IoU}$ is the IoU loss, N is the number of pixels in an image, s_i is the predicted value of the ith pixel in an image, and g_i is the targeted ground-truth value of the ith pixel in an image.

The SegFormer models were trained using the Adam optimizer. A 0.0001 learning rate was used, as well as early stopping based on validation loss for both SegFormer models. No data augmentation strategy was carried as part of training the SegFormer models. All training was implemented on a Windows 11 (Microsoft, Redmond, WA, USA) computer equipped with a GeForce RTX 2060 graphics

processing unit (NVIDIA, Santa Clara, CA, USA). Training of the SegFormer models was completed using Python 3.10.0 with PyTorch Lightning 1.8.6. Post-processing was implemented to ensure continuous layer boundaries and minimize the effect of isolated false positive regions (details are provided in Supplementary Material C).

We implemented fivefold cross-validation on the video and volume datasets independently. The training data were arranged five different ways, in each instance splitting the whole into training, validation, and test-sets. For each fold, 10% of the B-scans were assigned to the validation set, and 10% to the test-set. The training and validation sets were used for model training, and the test-sets were used for performance evaluation.

The test-set fivefold cross-validation performance for both the video and volume datasets was evaluated based on similarity metrics, as well as choroid boundaries mean absolute error (MAE) and choroid thickness difference (TD) between the manually segmented and corresponding automatically segmented frames. Equations 2 and 3 for MAE and TD, respectively, are provided below:

$$MAE = \frac{1}{m}\sum_{i=1}^{m}\left|y^{(i)} - \hat{y}^{(i)}\right| \tag{2}$$

$$TD = \frac{1}{m}\sum_{i=1}^{m}\left\|y_{CSI}^{(i)} - y_{BM}^{(i)}\right| - \left|\hat{y}_{CSI}^{(i)} - \hat{y}_{BM}^{(i)}\right\| \tag{3}$$

where m is the B-scan width and $y^{(i)}$ and $\hat{y}^{(i)}$ are the inferred and manually labeled vertical boundaries of Bruch's membrane (BM) or the choroid–sclera interface (CSI). Sørensen–Dice coefficient complement (Dice^C) and Jaccard coefficient complement (Jaccard^C) were used as similarity metrics. For our study, Dice^C and Jaccard^C of 0 indicated perfect overlap between the manually and automatically segmented regions, and 1 indicated no overlap. We also defined mathematical expressions to identify inaccurate segmentation and segmentation failure associated with subtle and gross segmented boundary aberrations, respectively (equations are provided in Supplementary Material D).

Beyond choroid segmentation, we produced masks of LA to calculate the CVI (details are provided in Supplementary Material E). The CVI was calculated as LA divided by total choroid layer area. The LA processing performance was assessed on the test-set of selected SegFormer models for both videos and volumes using similar methods as for choroid segmentation performance evaluation. Additional test-set performance evaluations relating to choroid layer and lumen segmentation are provided in Supplementary Material I. Subsequent temporal and spatial analyses were performed on the complete datasets, including the training data.

Temporal Analysis

Inference was only performed on B-scans that met noise specifications based on OCT device manufacturer-defined metrics. The SPECTRALIS OCT provides a quality score in decibels (dB) based on a signal-to-noise ratio estimate.[27] Only B-scans with a quality score ≥ 24 dB (0–40 dB score range, where 0 dB indicates no signal and 40 dB indicates excellent quality) and with an automatic real time frame averaging number ≥ 2 were considered. We also implemented our own signal-to-noise ratio and excluded B-scans with a ratio beneath 0.55. The signal-to-noise ratio equation (Equation 4) is provided below:

$$SNR = \frac{S}{\sigma} \tag{4}$$

where SNR is the signal-to-noise ratio, S is the mean, and σ is the standard deviation of the intensities in a B-scan. B-scans for which the inferred choroid region was located within 10% of the superior or inferior vertical edge of the image were excluded. Single B-scans with an inferred choroid area (CA) departing from the average of the manually segmented frames by ≥20% were also excluded.

OCT videos were unevenly sampled and frequency analysis was performed with Lomb–Scargle periodograms and spectrograms generated over a 0.1- to 4-Hz frequency range (transforms implementation details and calibration test results are provided in Supplementary Material G). Movies with fewer than 50 good-quality frames were discarded. To prevent large gaps in a video, we preserved only the longest video segment for which no zone of excluded frames amounting to greater than 1 second was present. Pulsatile choroidal thickness, LA, and CVI (ΔCT, ΔLA, and ΔCVI) were computed as done by Beaton et al.[20] First, the locations of peaks and valleys across time series were obtained, where the minimum distance between them is given by Equation 5:

$$d_{min} = \frac{T_{heart}}{3 \cdot M_{o,intervals}} \tag{5}$$

where d_{min} is the minimum distance between peaks and between valleys, T_{heart} is the heart period, and $M_{o,intervals}$ is the mode of the one-dimensional array of intervals between each element in a time series. Having obtained peak and valley locations, consecutive peaks between valleys and consecutive valleys between peaks were discarded. ΔCT, ΔLA, and ΔCVI were then defined as the difference between the median of all remaining peaks and the median of all remaining valleys. Each quantification result was divided into macular Early Treatment Diabetic Retinopathy Study (ETDRS) subfields (center, nasal inner, temporal inner, nasal outer, and temporal outer), in addition to a global level value.

A video was excluded entirely if more than 150 B-scans were under the signal-to-noise specification or met the edge exclusion criterion. Furthermore, a video with ΔCT far exceeding previously reported upper physiological values in any region was not kept. The scheme for exclusion based on ΔCT was implemented by Equation 6:

$$Cv = \begin{cases} 1 \text{ if } \Delta CT_r > \frac{CT_r}{CT_g} \cdot \Delta CT_{g,reference} \cdot \varepsilon, \\ 0 \text{ otherwise.} \end{cases} \tag{6}$$

where C_v is the choroid pulsatility-based video exclusion criterion (with 1 indicating exclusion and 0 indicating inclusion), ΔCT_r and CT_r are global or ETDRS region measurements, CT_g is the global measure, $\Delta CT_{g,reference}$ is a global constant of 20 µm, and ε represents an excess threshold of 3. Having obtained temporal choroid quantifications, we determine statistical significance of differences between pre- and post-spaceflight time points.

Investigative Ophthalmology & Visual Science

Spatial Analysis

For OCT volumes, the automatic real time averaging setting was 15 frames per B-scan. Following initial segmentation, smoothing of the surface of the CSI across each macular volume was implemented using a graph search algorithm similar to the one described by Mazzaferri et al.[21] The graph search algorithm was applied to each one of the cross-sectional images of the volume along the fast acquisition direction.

After delineating the region between the BM and a smoothed CSI, choroid volume (CV), luminal volume (LV), and the CVI were quantified (CT and LT are included in Supplementary Material N). In addition to a global level value, the result of each quantification was split into macular ETDRS subfields (center, superior inner, nasal inner, inferior inner, temporal inner, superior outer, nasal outer, inferior outer, and temporal outer).

For better visualization, we created square maps of CT, LT, and the CVI of 512 × 512 pixels by interpolating the total number of B-scans of every OCT volume, and we analyzed variation across time points. We determined the statistical significance of spatial choroid measurement differences between time points.

Repeatability

We evaluated the repeatability of choroid measurements using sets of OCT videos and volumes obtained in the same session by gathering the significance of differences. We calculated intraclass correlation coefficients and standard errors of measurement between these measures. Our repeatability evaluations are described and complete results are provided in Supplementary Materials J and K.

Statistical Analyses

Linear mixed models were used to determine the statistical significance of differences between measurements. For each linear mixed model, time points (or scans for repeatability analyses) were designated as the fixed effect. Subjects and eyes nested under each subject were specified as random effects.[28] The linear mixed models were implemented in R 4.3.1 (R Foundation for Statistical Computing, Vienna, Austria) using the lme4 (1.1.33) package. Significance values were gathered using the Kenward–Roger approximation.[29]

Results

SegFormer-Based Choroid Segmentation

To show choroid morphology changes in response to microgravity exposure, we retrained SegFormer models directly on astronaut OCT macular videos and volumes. We combined our segmentation with a simple strategy to analyze vascular changes. We manually labeled a 2% subset of the available images and assessed the test-set performance of our pipeline using different metrics.

We leveraged a dataset of OCT macular videos to compare pre- and post-spaceflight time-dependent variables obtained from astronauts. We used images centered at the macula from 12 individuals (nine males and three females; average age, 47 ± 9 years); one subject of the initial 13 was excluded based on video filtering criteria. Eight astronauts did not have prior spaceflight experience, three had completed Space Shuttle short-duration missions, and three had previous long-duration spaceflight experience (>4 months[30]). All preflight videos were obtained within a 9- to 1-month pre-spaceflight window, and all post-spaceflight videos within 2 to 30 days after spaceflight.

Figures 1a and 1d display illustrations of three individuals' manual and automated segmentations showing moderate-high to high correspondence for choroid and vascular lumen obtained from OCT videos. Mean Dice^C and Jaccard^C values for the test-set (Fig. 1b) were 0.044 ± 0.02 and 0.083 ± 0.03, respectively. Figure 1c provides segmentation MAE, expressed as the deviation of the boundary (in pixel units) from the labeled traces. It also shows TD, which represents the deviation of the layer thickness (in pixels) from the labeled layer. Test-set BM and CSI MAE values were 0.93 ± 0.3 pixels and 6.2 ± 2.7 pixels, respectively, and TD was 6.1 ± 2.7 pixels. Test-set LA mean Dice^C and mean Jaccard^C values were 0.32 ± 0.01 and 0.48 ± 0.09, respectively (Fig. 1e).

The performance was similar for the B-scans from OCT volumes (manual and automated segmentations are shown in Figs. 2a and 2d). This second set contained OCT volumes centered at the macula from six of the 12 astronauts featured in on-Earth videos (five males and one female; average age, 48 ± 9 years). Four astronauts did not have prior spaceflight experience, one had completed Space Shuttle short-duration missions, and two had previous long-duration spaceflight experience. The volumes were obtained from both eyes at up to six different time points before launch (launch – 21 to 18 months, launch – 9 to 6 months), during flight and before return (launch + 30 days, launch + 90 days, return – 30 days) and following spaceflight (return + 1 to 3 days). Test-set choroid segmentation mean Dice^C and mean Jaccard^C values for OCT macular volumes were 0.057 ± 0.02 and 0.11 ± 0.04, respectively (Fig. 2b). Test-set BM and CSI MAE values were 1.2 ± 0.3 pixels and 8 ± 4.2 pixels, respectively, and TD was 7.9 ± 3.9 pixels (Fig. 2c). Test-set LA mean Dice^C and mean Jaccard^C values were 0.39 ± 0.07 and 0.55 ± 0.07, respectively (Fig. 2e). Additional choroid layer segmentation and lumen segmentation performance evaluations are provided in Supplementary Figures S10 and S11.

Quantification of Choroid Pulsatile Changes

We investigated the presence of spaceflight-related changes in choroid pulsatility. For this, as we have done in the past,[20] we obtained videos of OCT images of about 1 minute, acquired at 14.25 Hz. The built-in eye tracker of the OCT device was used to ensure that the same location in the macula was sampled throughout the video. The acquisition was automatically halted when a patient moved, only resuming after the laser was repositioned. Our choroid quantification approaches were implemented on the videos, yielding time series that displayed morphological changes at the frequency of the heart. Because images were not sampled at a constant rate, Lomb–Scargle periodograms and spectrograms of normalized power were expected to show peaks in the heart rate vicinity. Detection of those peaks, as illustrated in Figures 3d to 3f, serves as quality control for segmentation. Narrow and prominent maxima can often be seen for CT, LA, and CVI (see also Supplementary Figs. S18 and S19, second and third columns).

We found a global CT averaged over movie durations significant increase of 15 ± 30 µm or 5.3% ($P = 0.02$, linear

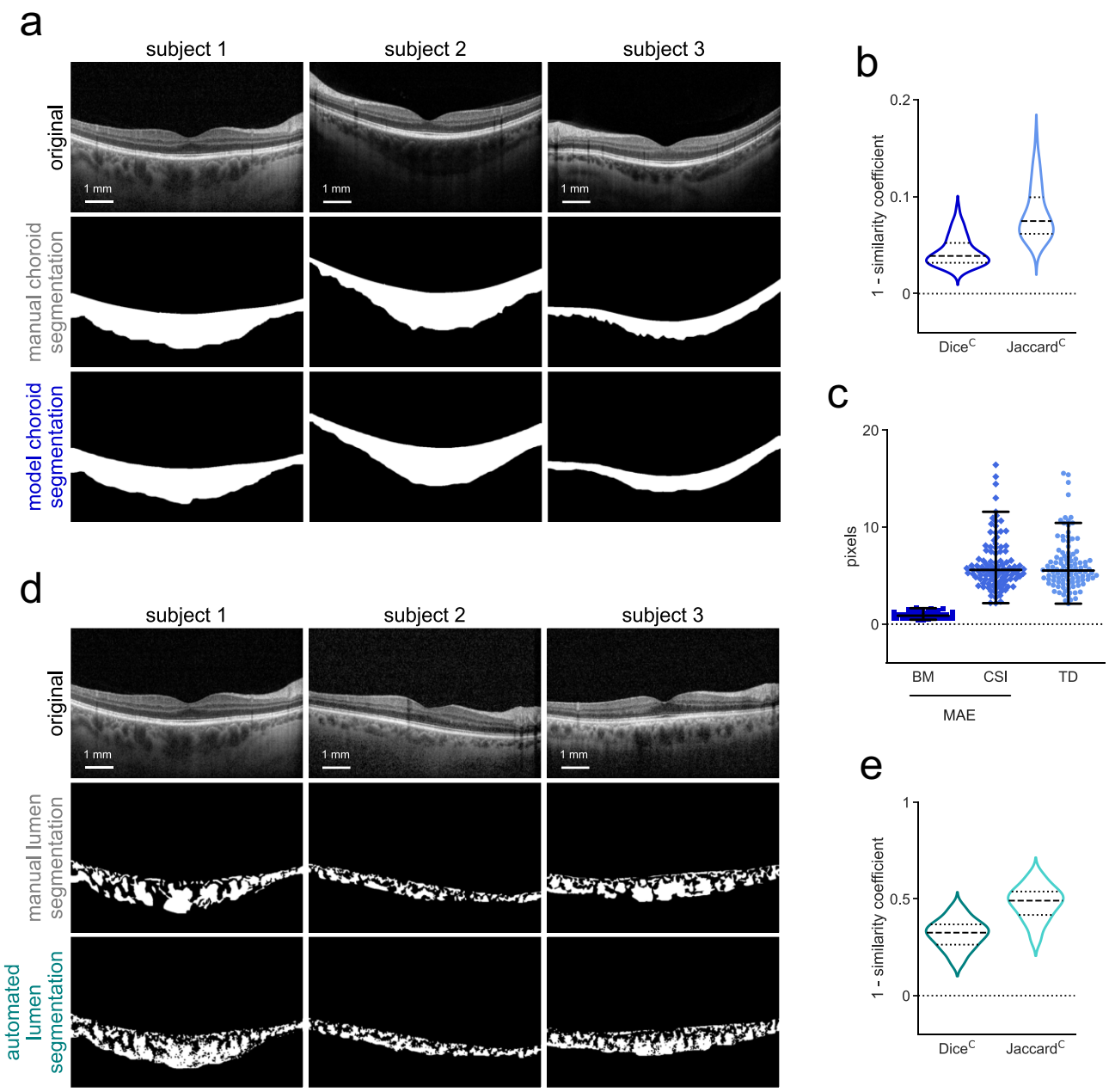

Figure 1. Choroid layer and lumen segmentation performance evaluation for OCT videos. (**a**) Original OCT video B-scans and binary choroid layer segmentation masks for three subjects obtained manually and through model inference. (**b**) Violin plots displaying test-set Dice^C and Jaccard^C values between manual and model choroid layer segmentations. (**c**) Swarm plots of test-set BM and CSI MAEs and average TDs between manual and model choroid layer segmentations. (**d**) Original OCT video B-scans and binary lumen segmentation masks for three subjects obtained manually and automatically. (**e**) Violin plots displaying test-set Dice^C and Jaccard^C values between manual and automated lumen segmentations.

mixed model) from pre- to post-spaceflight, and global LA significant increase of 0.12 ± 0.3 mm^2 or 7.9% (P = 0.03, linear mixed model) (Figs. 3a, 3b), but no change in global CVI (Fig. 3c). For the analysis of the amplitude of pulsatile fluctuations, no significant differences in ΔCT or ΔCVI were found globally (Figs. 3a, 3c). As shown in Figure 3b, global ΔLA did show a significant increase from pre- to post-spaceflight of 0.058 ± 0.13 mm^2 or 25% (P = 0.03, linear mixed model). We provide baseline pre-spaceflight results of our choroid quantification methods for OCT videos from astronaut eyes, including their ETDRS subfield equivalents, in Supplementary Table S6. The ETDRS subfield equivalents of measures displayed in Figures 3a to 3c are provided in Supplementary Figure S17 and significance in Supplementary Table S8.

Spatial Choroid Changes Associated With Long-Duration Spaceflight

We extended our choroid quantification techniques to OCT volumes, for which large variations were expected in astro-

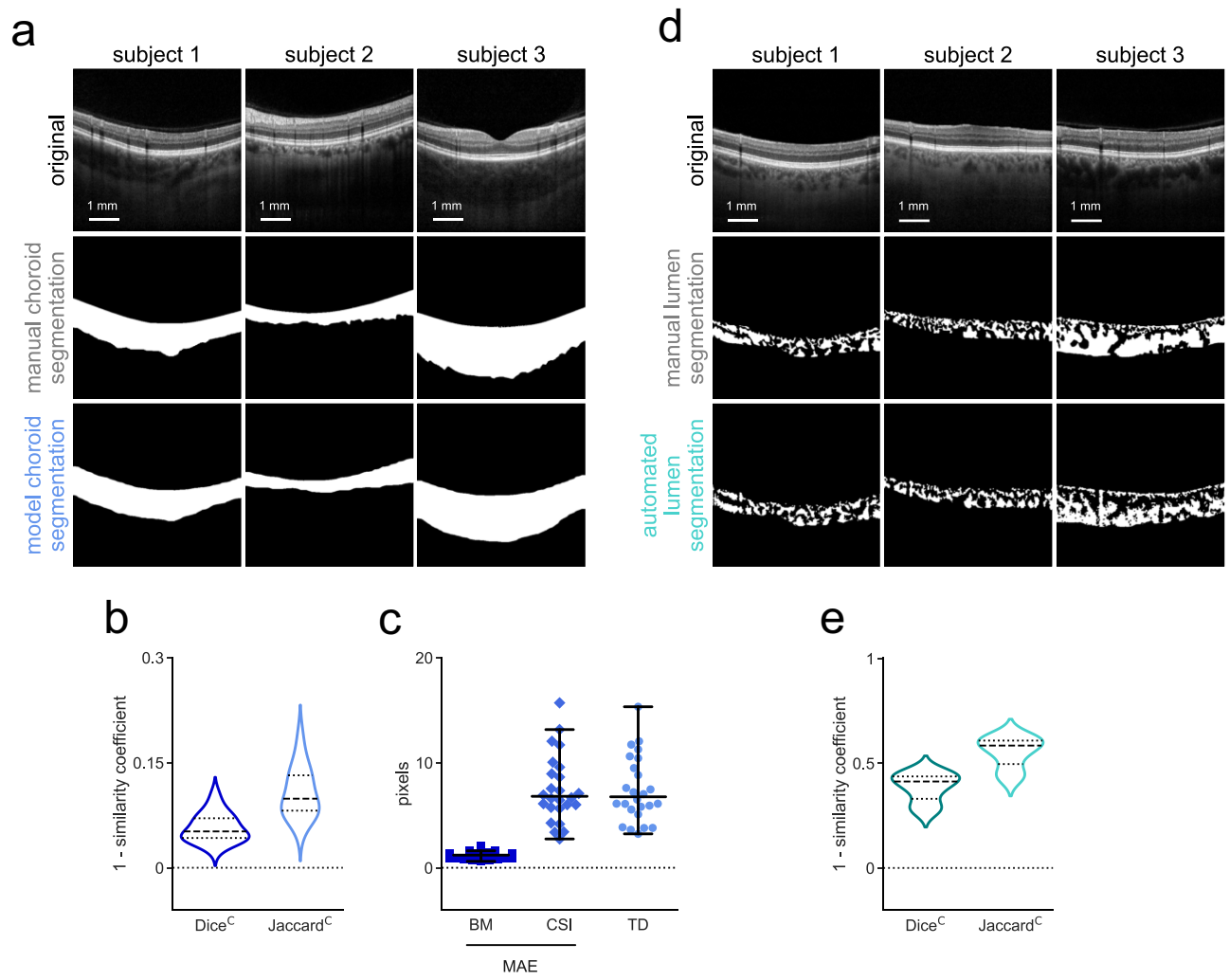

Figure 2. Choroid layer and lumen segmentation performance evaluation for OCT volumes. (**a**) Original OCT volume B-scans and binary choroid layer segmentation masks for three subjects obtained manually and through model inference. (**b**) Violin plots displaying test-set Dice^C and Jaccard^C values between manual and model choroid layer segmentations. (**c**) Swarm plots of test-set BM and CSI MAEs and average TDs between manual and model choroid layer segmentations. (**d**) Original OCT volume B-scans and binary lumen segmentation masks for three subjects obtained manually and automatically. (**e**) Violin plots displaying test-set Dice^C and Jaccard^C values between manual and automated lumen segmentations.

nauts. Each volume is made up of 97 or 193 B-scans. In addition to obtaining cross-sectional image segmentation performance, we generated maps exposing choroid thickness (CT) topography and vascular patterns. Choroid vessel patterns were readily observable on LT and CVI maps in OCT volumes (Fig. 4d). For all eyes, there was a correspondence between CT and LT maps, with thicker choroid regions generally translating to thicker luminal regions. Different degrees of retinal vessel shadow artifacts were discernable in most scans.

When comparing individual time points with preflight, there were significant differences for global CV and LV (Figs. 4a, 4b) for all measurements. The same comparison for global CVI measurements indicated significant differences for inflight time points and normal values for return + 1 to 3 days (Fig. 4c). We provide baseline results of our choroid quantification methods for OCT volumes from astronauts, including their ETDRS subfield equivalents, in Supplementary Table S7. The ETDRS subfield equivalents of measures displayed in Figures 4a to 4c are provided in Supplementary Material N and significance values in Supplementary Tables S9 to S12.

Discussion

In addition to an increase in CT within the macular region during the month that follows long-duration spaceflight, we found an increase in the area corresponding to the lumen. Our results also indicate that, although pulsatile fluctuations in CT did not change compared to preflight when measured within 30 days of return, the amplitude of pulsatile fluctuations in LA increased. During missions, we observed a global increase in the space occupied by lumen relative to the whole choroid layer across the macular plane.

Consistent with our results, a study that measured macular CT preflight and during spaceflight showed a 35-µm CT increase.[31] Previous reports demonstrated similar increases in peripapillary CT. Laurie et al.[32] found a mean peripapillary CT increase of 27 µm during spaceflight compared to

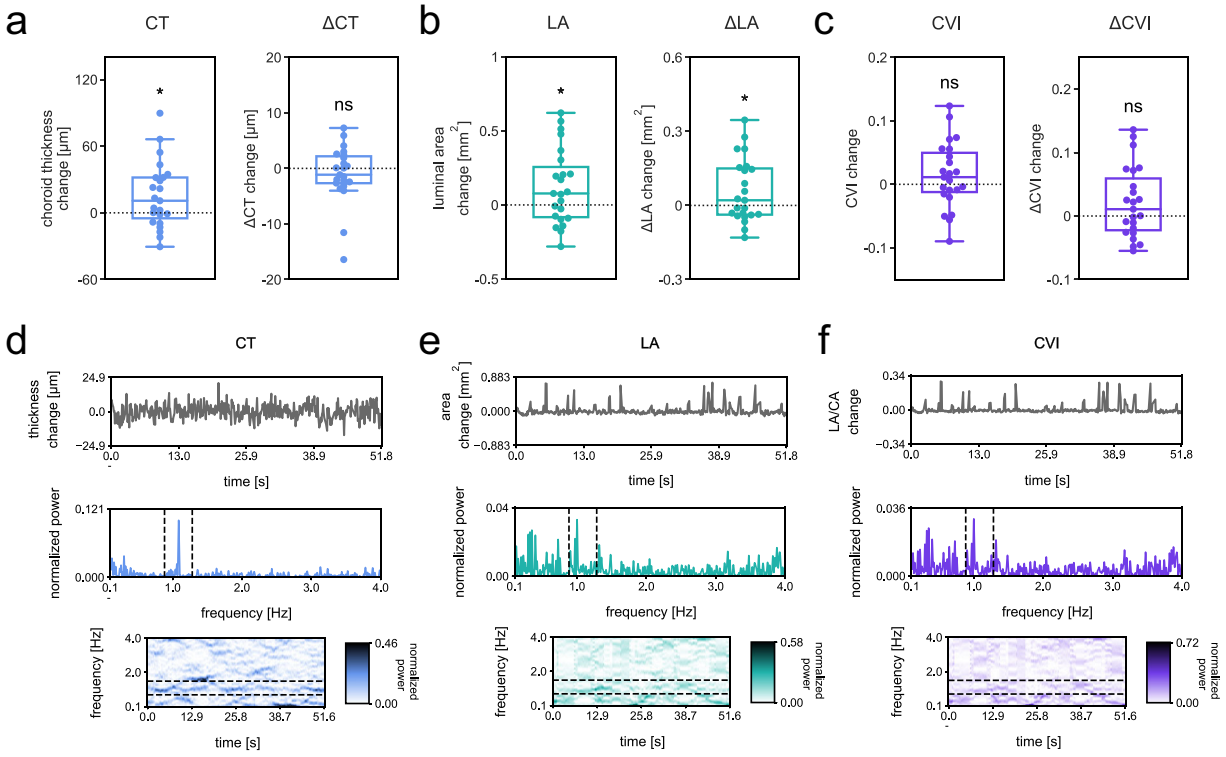

Figure 3. (a–c) Temporal choroid pulsatile changes. Difference box plots between post- and pre-spaceflight for CT and ΔCT measurements obtained over the selected segments for all astronaut eyes (**a**), LA and ΔLA (**b**), and CVI and ΔCVI (**c**). ns, nonsignificant. *$P < 0.05$, linear mixed model. (**d–f**) Selected segment time series, frequency, and joint time–frequency transforms for one subject's eye acquisition displaying the behavior of CT (**d**), LA (**e**), and CVI (**f**). The *top row* features time series; the *second row* features Lomb–Scargle periodograms; and the *third row* features Lomb–Scargle spectrograms. *Dashed lines* on the periodograms and spectrograms show values that are ±20% and ±40% of the oximeter measured heart rate value, respectively.

preflight. Macias et al.[6] observed progressive peripapillary choroid thickening over the course of long-duration spaceflight, with a mean increase of 43 µm at 150 days. In line with our findings for CT at the macula, they also showed still significantly increased peripapillary CT at 30 days following return to Earth. Unlike the present work, previous studies were limited to measuring CT from a single image. Here, we complement previous reports by adding maps of thickness change, as well as an analysis of how lumen and CVI evolve and their response to cardiac pulsation.

Several mechanisms have been proposed to account for increased CT upon microgravity exposure. They include cephalad fluid shift resulting in venous congestion and accumulation of blood in the choroid,[3,5,33] as well as persistent buildup of choroidal interstitial fluid in the peripapillary area.[2,34] In line with the posited cephalad fluid shift mechanism, a mathematical model of the cardiovascular response to long-duration spaceflight predicted increased upper body blood volume.[35]

Determining the source of optic disc edema observed in SANS has been described as challenging using available technology and approaches to data analysis.[6] The results of finite element modeling suggest a relationship between choroid anatomy, increased pulsatile choroid volume fluctuation, prelaminar neural tissue strains, and the development of edema.[2,10] Our study directly shows increased amplitude of pulsatile fluctuation of the space occupied by choroid vessels at the macula after spaceflight. The finding opens the possibility of investigating whether a ΔLA elevation can also be observed in the peripapillary region. A relationship could in turn be explored between the latter and peripapillary retinal thickness increase in SANS. Pulsatile deformation of the optic nerve head may be assessed using OCT[36] and could also be studied in relation to peripapillary choroid pulsatile changes, helping substantiate finite element modeling predictions.

Studies have linked the development of edema in SANS with single nucleotide polymorphisms (SNPs).[37,38] A lower enzyme functional activity in the one-carbon pathway can increase B-vitamin requirements and the risk of vitamin insufficiency.[39] The insufficiency may lead to the generation of reactive oxygen species,[40,41] with a deleterious effect on interendothelial junctions and a rise in protein and fluid leakage into the interstitial space.[42,43] A significant association has been found between choroid thickness change in SANS and peripapillary retinal thickness increase,[8] an imaging biomarker of disc edema,[44,45] and common factors may underly variation in their manifestation. Specifically, both individual differences in posterior segment anatomy[10] and SANS-relevant SNPs[37,38] could contribute to the degree of choroid morphological changes observed.

The application of lower body negative pressure has been explored as a means of mitigating the effects of cephalad fluid shift in SANS. Although lower body nega-

Investigative Ophthalmology & Visual Science

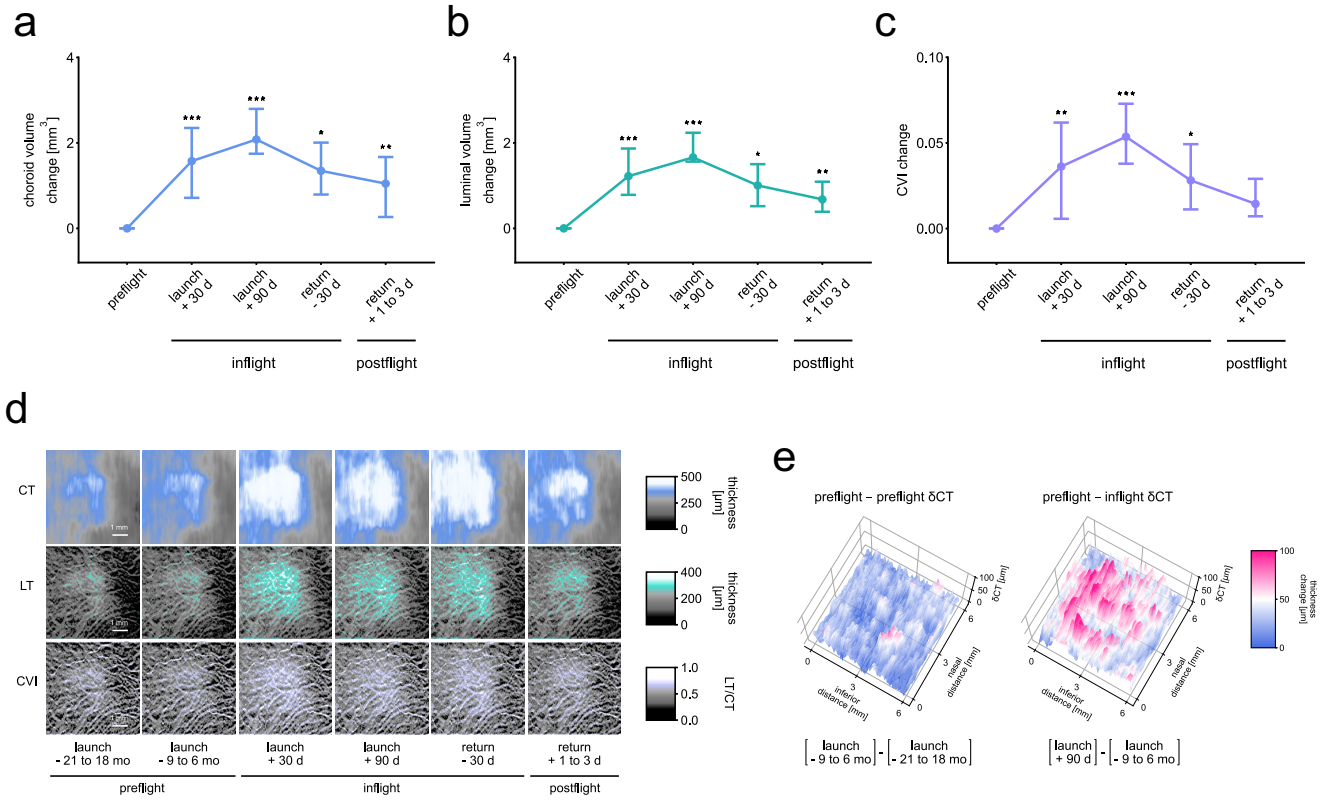

Figure 4. Spatial choroid changes. (**a**–**c**) Line charts showing changes over preflight, inflight, and postflight time points for all astronaut eyes for choroid volume (**a**), luminal volume (**b**), and CVI (**c**). *Error bars* show the difference interquartile range and *dots* indicate the mean difference. *$P < 0.05$, **$P < 0.01$, ***$P < 0.001$, linear mixed model. (**d**) Maps of CT, LT, and CVI over preflight, inflight, and postflight time points for one subject's eye. The *top row* displays CT maps, the *middle row* displays LT maps, and the *bottom row* displays CVI maps. (**e**) Surface plots of the difference between two preflight CT maps (launch – 21 to 18 months and launch – 9 to 6 months) (*left*) and the difference between preflight and inflight CT maps (launch – 9 to 6 months and launch + 90 days) (*right*) for the same subject's eye acquisitions. δCT, choroid thickness change.

tive pressure was shown to decrease intraocular pressure in astronauts during spaceflight, no change in macular CT was observed.[31] Numerical modeling suggests that, under microgravity conditions, less rigid vessels are subjected to increased transmural pressure and greater than normal volume.[46] An artificial gravity experiment achieved partial alleviation of mice retinal tissue damage associated with weightlessness exposure.[47,48] The effects of artificial gravity on the state of the choroid have not been explored, and the need for precise and reliable methods of assessing SANS-related eye alterations to validate its effectiveness as a countermeasure has been emphasized.[48] The approaches we developed for the measurement of pulsatile and volume choroid changes represent a step in this direction.

Head-down tilt bed rest has been explored as a SANS analog and toward studying the effect of countermeasures. There have been conflicting reports about the impact of head-down tilt bed rest on CT in the peripapillary and macular regions. Some studies have shown significantly increased CT in response to head-down tilt bed rest,[49–51] with others showing no CT alteration.[52,53] Choroid changes observed were generally lower in the analog than those resulting from microgravity exposure,[52,54] which is consistent with our observation of the differences reached at 90 days following launch. Unlike during spaceflight, significantly increased intraocular pressure has been reported in head-down tilt bed rest studies.[49,51–53] When comparing head-down tilt bed rest and prolonged microgravity exposure with respect to the development of optic disc edema, differences in the combined effects of posterior segment anatomy, pulsatile choroid volume fluctuation, and intraocular pressure may be at play, as predicted by finite element modeling.[10]

A relationship between venous congestion in SANS and raised intracranial pressure has been proposed.[55] In contrast with the pervasiveness of choroid enlargement in space, the manifestation of visible choroidal folds may depend on intracranial hypertension and individual microanatomical variation. From a biomechanical perspective, an early exploration of ocular rigidity in a private astronaut suggested that it decreases following spaceflight,[12] and this was recently confirmed in professional astronauts.[11] It has been suggested that thickening of the choroid could extend scleral collagen and modify its properties, resulting in the observed lowered postflight ocular rigidity.

Pulsatile choroid volume fluctuation correlates inversely with the measurement of ocular rigidity performed using an invasive procedure.[25] Combined with additional measurements, our choroid layer segmentation method has the potential to improve upon a key element in the computation of ocular rigidity and delve deeper into its relationship to SANS. Furthermore, the significant postflight global and localized increases in ΔLA we observed could be associated with increased choroidal vessel compliance following sustained greater than normal volume during long-duration

spaceflight. The techniques we described here offer novel approaches and opportunities to explore SANS etiology and to implement effective strategies against risks linked with extended space travel.

Our study is not without some limitations, and they should be highlighted. First, our results suggest that there is considerable variability in model predictions, and they systematically underestimate the size of the choroid space. In spite of the limitation, the BM and CSI MAE, choroid TD, and Dice^{C} values for OCT videos and volumes were comparable with reported values obtained using similar methods on myopic children and adults.[18,56] Similar performance was also achieved when compared with the segmentation of healthy choroids using convolutional neural networks.[57,58] Manual and model segmentations produced well-correlated measurements across the available range of choroid thicknesses. Despite the correlations, the CSI can be challenging to identify visually in very thick choroids, and this could have adversely impacted our results. Unlike with learned choroid segmentation, with our automated lumen quantification approach there was a systematic area overestimation. Perhaps this is due at least in part to the difficulty of capturing very small luminal detail by hand. Using a scheme previously described,[59] luminal area segmentation achieved moderate-high similarity. Nevertheless, it did not perform as well as choroid segmentation and showed sizable variability.

In addition to segmentation performance considerations, our sample size is modest, and a larger number of participants would have enabled us to achieve a superior level of power. The significant changes we observed should be interpreted cautiously and with consideration of our repeatability assessment. The time interval between preflight acquisitions and launch was not considered as a fixed effect in the linear mixed models when analyzing OCT videos. We recognize that the exclusion of this variable as a fixed effect represents a limitation of our approach. Due in part to our sample size constraint, participants were not grouped based on their genetic profile or flight experience. We could address these limitation in the future by using the approaches we developed to determine whether individuals with SANS-relevant SNPs or prior flight experience demonstrate the same or greater choroid morphology changes in response to microgravity. Importantly, their relationship with peripapillary retinal thickness alterations could be elucidated. A control group of astronauts who remained on Earth was not included as part of our study. In support of our approach, no significant differences were found in our evaluation of repeatability. There was also generally a marked distinction in the magnitude of the difference between two preflight time points and when comparing our baseline with subsequent time points.

Finally, there were additional factors which could have affected our results. The time of day of initial and subsequent OCT acquisitions was not always consistent across time points, and this could have impacted our findings. In most instances where significance was found, changes in response to microgravity exposure reached magnitudes beyond what could reasonably be anticipated from diurnal fluctuations alone. The results corresponding to changes in metrics obtained from OCT videos and OCT volumes were also not adjusted for axial length. We acknowledge the possibility that establishing a relationship between choroid-based metrics and axial length for our data could help reveal important physiological insights.

Conclusions

In conclusion, neuro-ophthalmic findings in SANS, including optic disc edema, constitute important risks for astronauts and their missions. Weightlessness results in rapid choroidal expansion, which may partially account for concerning SANS findings. Macular region luminal area and the amplitude of its pulsatile fluctuation were both increased compared to preflight within 30 days after long-duration spaceflight. During long-duration spaceflight, there is a global increase in both the choroid layer and the relative space occupied by lumen inside the choroid across the macular plane.

Acknowledgments

The authors thank NASA and ESA for coordination and infrastructure.

Supported by the Canadian Space Agency, Canadian Institutes of Health Research, and Fonds de Recherche en Ophtalmologie de l'Université de Montréal (FROUM), as well as a scholarship from Fonds de Recherche du Québec Santé (MMS).

Disclosure: **C. Bélanger Nzakimuena**, None; **M. Masís Solano**, None; **R. Marcotte-Collard**, None; **M.R. Lesk**, None; **S. Costantino**, None

References

1. Martin Paez Y, Mudie LI, Subramanian PS. Spaceflight associated neuro-ocular syndrome (SANS): a systematic review and future directions. *Eye Brain*. 2020;12:105–117.
2. Ong J, Tarver W, Brunstetter T, et al. Spaceflight associated neuro-ocular syndrome: proposed pathogenesis, terrestrial analogues, and emerging countermeasures. *Br J Ophthalmol*. 2023;107(7):895–900.
3. Lee AG, Mader TH, Gibson CR, Tarver W. Space flight–associated neuro-ocular syndrome. *JAMA Ophthalmol*. 2017;135(9):992–994.
4. Lee AG, Mader TH, Gibson CR, Brunstetter TJ, Tarver WJ. Space flight-associated neuro-ocular syndrome (SANS). *Eye (Lond)*. 2018;32(7):1164–1167.
5. Lee AG, Mader TH, Gibson CR, et al. Spaceflight associated neuro-ocular syndrome (SANS) and the neuro-ophthalmologic effects of microgravity: a review and an update. *NPJ Microgravity*. 2020;6(1):7.
6. Macias BR, Patel NB, Gibson CR, et al. Association of long-duration spaceflight with anterior and posterior ocular structure changes in astronauts and their recovery. *JAMA Ophthalmol*. 2020;138(5):553–559.
7. Patel ZS, Brunstetter TJ, Tarver WJ, et al. Red risks for a journey to the red planet: the highest priority human health risks for a mission to mars. *NPJ Microgravity*. 2020;6(1):33.
8. Sibony PA, Laurie SS, Ferguson CR, et al. Ocular deformations in spaceflight-associated neuro-ocular syndrome and idiopathic intracranial hypertension. *Invest Ophthalmol Vis Sci*. 2023;64(3):32.
9. Mrejen S, Spaide RF. Optical coherence tomography: imaging of the choroid and beyond. *Surv Ophthalmol*. 2013;58(5):387–429.
10. Feola AJ, Nelson ES, Myers J, Ross Ethier C, Samuels BC. The impact of choroidal swelling on optic nerve head deformation. *Invest Ophthalmol Vis Sci*. 2018;59(10):4172–4181.
11. Solano MM, Dumas R, Lesk MR, Costantino S. Ocular biomechanical responses to long-duration spaceflight. *IEEE Open J Eng Med Biol*. 2024;6:127–132.
12. Solano MM, Nzakimuena CB, Dumas R, Lesk MR, Costantino S. Ocular rigidity and choroidal thickness changes in

response to microgravity: a case study. *Am J Ophthalmol Case Rep*. 2023;32:101940.
13. Mader TH, Gibson CR, Lee AG. Choroidal folds in astronauts. *Invest Ophthalmol Vis Sci*. 2016;57(2):592.
14. Laviers H, Zambarakji H. Enhanced depth imaging-oct of the choroid: a review of the current literature. *Graefes Arch Clin Exp Ophthalmol*. 2014;252:1871–1883.
15. Wu L, Masis M, Hernandez-Bogantes E. Choroidal imaging with spectral-domain optical coherence tomography, enhanced depth imaging may lead to a broader understanding of the pathogenesis of several eye diseases. *Retina Surg Glob Perspect*. 2011;114:39–42.
16. Singh SR, Vupparaboina KK, Goud A, Dansingani KK, Chhablani J. Choroidal imaging biomarkers. *Surv Ophthalmol*. 2019;64(3):312–333.
17. Sui X, Zheng Y, Wei B, et al. Choroid segmentation from optical coherence tomography with graph-edge weights learned from deep convolutional neural networks. *Neurocomputing*. 2017;237:332–341.
18. Xuan M, Wang W, Shi D, et al. A deep learning–based fully automated program for choroidal structure analysis within the region of interest in myopic children. *Transl Vis Sci Technol*. 2023;12(3):22.
19. Zhang H, Yang J, Zheng Ce, Zhao S, Zhang A. Annotation-efficient learning for oct segmentation. *Biomed Opt Express*. 2023;14(7):3294–3307.
20. Beaton L, Mazzaferri J, Lalonde F, et al. Non-invasive measurement of choroidal volume change and ocular rigidity through automated segmentation of high-speed oct imaging. *Biomed Opt Express*. 2015;6(5):1694–1706.
21. Mazzaferri J, Beaton L, Hounye G, Sayah DN, Costantino S. Open-source algorithm for automatic choroid segmentation of oct volume reconstructions. *Sci Rep*. 2017;7(1):42112.
22. Parvaiz A, Khalid MA, Zafar R, Ameer H, Ali M, Fraz MM. Vision transformers in medical computer vision—a contemplative retrospection. *Eng Appl Artif Intell*. 2023;122:106126.
23. Thisanke H, Deshan C, Chamith K, Seneviratne S, Vidanaarachchi R, Herath D. Semantic segmentation using vision transformers: a survey. *Eng Appl Artif Intell*. 2023;126:106669.
24. Agrawal R, Ding J, Sen P, et al. Exploring choroidal angioarchitecture in health and disease using choroidal vascularity index. *Prog Retin Eye Res*. 2020;77:100829.
25. Sayah DN, Descovich D, Costantino S, Lesk MR. The association between the pulsatile choroidal volume change and ocular rigidity. *Ophthalmol Sci*. 2024;6(1):100576.
26. Xie E, Wang W, Yu Z, Anandkumar A, Alvarez JM, Luo P. SegFormer: simple and efficient design for semantic segmentation with transformers. *Adv Neural Inf Process Syst*. 2021;34:12077–12090.
27. Balasubramanian M, Bowd C, Vizzeri G, Weinreb RN, Zangwill LM. Effect of image quality on tissue thickness measurements obtained with spectral domain-optical coherence tomography. *Opt Express*. 2009;17(5):4019–4036.
28. Fan Q, Teo Y-Y, Saw S-M. Application of advanced statistics in ophthalmology. *Invest Ophthalmol Vis Sci*. 2011;52(9):6059–6065.
29. Luke SG. Evaluating significance in linear mixed-effects models in R. *Behav Res Methods*. 2017;49:1494–1502.
30. Lee SMC, Ribeiro LC, Martin DS, et al. Arterial structure and function during and after long-duration spaceflight. *J Appl Physiol*. 2020;129(1):108–123.
31. Greenwald SH, Macias BR, Lee SMC, et al. Intraocular pressure and choroidal thickness respond differently to lower body negative pressure during spaceflight. *J Appl Physiol*. 2021;131(2):613–620.
32. Laurie SS, Lee SMC, Macias BR, et al. Optic disc edema and choroidal engorgement in astronauts during spaceflight and individuals exposed to bed rest. *JAMA Ophthalmol*. 2020;138(2):165–172.
33. Mader TH, Gibson CR, Caputo M, et al. Intraocular pressure and retinal vascular changes during transient exposure to microgravity. *Am J Ophthalmol*. 1993;115(3):347–350.
34. Wostyn P, Gibson CR, Mader TH. Optic disc edema in astronauts from a choroidal point of view. *Aerosp Med Hum Perform*. 2022;93(4):396–398.
35. Gallo C, Ridolfi L, Scarsoglio S. Cardiovascular deconditioning during long-term spaceflight through multiscale modeling. *NPJ Microgravity*. 2020;6(1):27.
36. Solano MM, Richer E, Cheriet F, Lesk MR, Costantino S. Mapping pulsatile optic nerve head deformation using OCT. *Ophthalmol Sci*. 2022;2(4):100205.
37. Zwart SR, Gibson CR, Mader TH, et al. Vision changes after spaceflight are related to alterations in folate-and vitamin B-12-dependent one-carbon metabolism. *J Nutr*. 2012;142(3):427–431.
38. Zwart SR, Gregory JF, Zeisel SH, et al. Genotype, B-vitamin status, and androgens affect spaceflight-induced ophthalmic changes. *FASEB J*. 2016;30(1):141.
39. Zwart SR, Gibson CR, Gregory JF, et al. Astronaut ophthalmic syndrome. *FASEB J*. 2017;31(9):3746–3756.
40. Katusic ZS. Vascular endothelial dysfunction: does tetrahydrobiopterin play a role? *Am J Physiol Heart Circ Physiol*. 2001;281(3):H981–H986.
41. Moens AL, Champion HC, Claeys MJ, et al. High-dose folic acid pretreatment blunts cardiac dysfunction during ischemia coupled to maintenance of high-energy phosphates and reduces postreperfusion injury. *Circulation*. 2008;117(14): 1810–1819.
42. Hadi HAR, Carr CS, Suwaidi JAl. Endothelial dysfunction: cardiovascular risk factors, therapy, and outcome. *Vasc Health Risk Manag*. 2005;1(3):183–198.
43. Moens AL, Vrints CJ, Claeys MJ, et al. Mechanisms and potential therapeutic targets for folic acid in cardiovascular disease. *Am J Physiol Heart Circ Physiol*. 2008;294(5):H1971–H1977.
44. Menke MN, Feke GT, Trempe CL. OCT measurements in patients with optic disc edema. *Invest Ophthalmol Vis Sci*. 2005;46(10):3807–3811.
45. Nguyen AM, Balmitgere T, Bernard M, et al. Detection of mild papilloedema using spectral domain optical coherence tomography. *Br J Ophthalmol*. 2012;96(3):375–379.
46. Lan M, Phillips SD, Archambault-Leger V, et al. Proposed mechanism for reduced jugular vein flow in microgravity. *Physiol Rep*. 2021;9(8):e14782.
47. Mao XW, Byrum S, Nishiyama NC, et al. Impact of spaceflight and artificial gravity on the mouse retina: biochemical and proteomic analysis. *Int J Mol Sci*. 2018;19(9): 2546.
48. Waisberg E, Ong J, Masalkhi M, Shimada K, Lee AG. Artificial gravity as a potential countermeasure for spaceflight associated neuro-ocular syndrome. *Eye (Lond)*. 2024;38(15):2847–2848.
49. Laurie SS, Vizzeri G, Taibbi G, et al. Effects of short-term mild hypercapnia during head-down tilt on intracranial pressure and ocular structures in healthy human subjects. *Physiol Rep*. 2017;5(11):e1330.
50. Lawley JS, Babu G, Janssen SLJE, et al. Daily generation of a footward fluid shift attenuates ocular changes associated with head-down tilt bed rest. *J Appl Physiol*. 2020;129(5):1220–1231.
51. Shinojima A, Iwasaki K-J, Aoki K, Ogawa Y, Yanagida R, Yuzawa M. Subfoveal choroidal thickness and foveal retinal thickness during head-down tilt. *Aviat Space Environ Med*. 2012;83(4):388–393.

Investigative Ophthalmology & Visual Science

52. Laurie SS, Greenwald SH, Marshall-Goebel K, et al. Optic disc edema and chorioretinal folds develop during strict 6° head-down tilt bed rest with or without artificial gravity. *Physiol Rep*. 2021;9(15):e14977.
53. Pardon LP, Cheng H, Chettry P, Patel NB. Optic nerve head morphological changes over 12 hours in seated and head-down tilt postures. *Invest Ophthalmol Vis Sci*. 2020;61(13):21.
54. Ong J, Lee AG, Moss HE. Head-down tilt bed rest studies as a terrestrial analog for spaceflight associated neuro-ocular syndrome. *Front Neurol*. 2021;12:648958.
55. Mader TH, Gibson CR, Pass AF, et al. Optic disc edema, globe flattening, choroidal folds, and hyperopic shifts observed in astronauts after long-duration space flight. *Ophthalmology*. 2011;118(10):2058–2069.
56. Wang Y, Yang Z, Liu X, et al. PGKD-net: prior-guided and knowledge diffusive network for choroid segmentation. *Artif Intell Med*. 2024;150:102837.
57. Mao X, Zhao Y, Chen B, et al. Deep learning with skip connection attention for choroid layer segmentation in oct images. In: *Proceedings of the 42nd Annual International Conferences of the IEEE Engineering in Medicine & Biology Society (EMBC)*. Piscataway, NJ: Institute of Electrical and Electronics Engineers, 2020:1641–1645.
58. Wu W, Gong Y, Hao H, et al. Choroidal layer segmentation in oct images by a boundary enhancement network. *Front Cell Dev Biol*. 2022;10:1060241.
59. Wilson SM, Bautista A, Yen M, Lauderdale S, Eriksson DK. Validity and reliability of four language mapping paradigms. *NeuroImage Clin*. 2017;16:399–408.

Investigative Ophthalmology & Visual Science